



Effective photocatalytic H_2O_2 production under visible light irradiation at $g\text{-}C_3N_4$ modulated by carbon vacancies

Shuna Li^{a,b}, Guohui Dong^{a,*}, Reshalaiti Hailili^a, Liping Yang^a, Yingxuan Li^a, Fu Wang^a, Yubin Zeng^{b,*}, Chuanyi Wang^{a,b,*}

^a Laboratory of Environmental Sciences and Technology, Xinjiang Technical Institute of Physics & Chemistry, Key Laboratory of Functional Materials and Devices for Special Environments, Chinese Academy of Sciences, Urumqi 830011, China

^b School of Power and Mechanical Engineering, Wuhan University, Hubei 430072, China

ARTICLE INFO

Article history:

Received 12 January 2016

Received in revised form 27 February 2016

Accepted 2 March 2016

Available online 4 March 2016

Keywords:

Photocatalysis

Hydrogen peroxide

Carbon vacancy

$g\text{-}C_3N_4$

Oxygen reduction

ABSTRACT

Hydrogen peroxide (H_2O_2) is of great significance in biological and environmental processes as well as in chemical industry. Even though anthraquinone autoxidation (AO) process has been the major artificial way to produce H_2O_2 , its energy cost and non-green nature have been motivating people to develop more efficient, economic and green technologies as alternatives. Here we demonstrated that photocatalytic H_2O_2 production at $g\text{-}C_3N_4$ could be improved by as much as 14 times in the absence of organic scavenger through a carbon vacancy-based strategy. Both the experimental and theoretical calculation results indicated that the creation of carbon vacancies could reduce the symmetry of $g\text{-}C_3N_4$ and produce the effect of electron delocalization. This will allow $g\text{-}C_3N_4$ to possess more excitable electrons and a narrower band gap. On the other hand, carbon vacancies provided more sites to adsorb molecular oxygen and thereby help electrons transfer from $g\text{-}C_3N_4$ to the surface adsorbed O_2 . More interestingly, the presence of carbon vacancies changed the H_2O_2 generation pathway from a two-step single-electron indirect reduction to an one-step two-electron direct reduction. This study could not only develop a novel strategy to improve the H_2O_2 production activity of semiconductors, but also shed light on the deep understanding of the role played by surface defect structure on photocatalytic activity of semiconductor photocatalysts.

© 2016 Elsevier B.V. All rights reserved.

1. Introduction

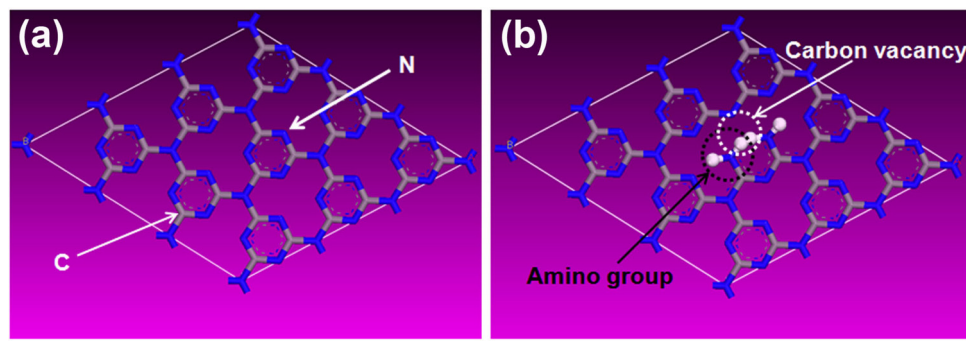
Hydrogen peroxide (H_2O_2) is an extremely versatile and useful agent. It is widely used in biological process, environmental remediation and chemical industry [1–3]. In the field of environmental remediation, H_2O_2 is a potent oxidant, which can directly or indirectly (in combination with other technology) oxidize a variety of organic or inorganic pollutants [4–6]. Since its reaction products are H_2O and O_2 only, H_2O_2 can also serve as an environmentally safe oxidant with numerous industrial applications including chemical syntheses, paper bleaching, textile bleaching and detergents production [7–10]. At present, the main methods for large-scale production of H_2O_2 include anthraquinone autoxidation, oxidation of alcohols and electrochemical synthesis [11–13]. However, these methods can hardly be considered as green ones due to the

consumption of a large amount of energy or organic solvent. In addition, H_2O_2 extracted from these systems may be contaminated by organic impurities. Therefore, it is highly desirable to develop efficient, economical and green technologies for the production of H_2O_2 .

Recently, H_2O_2 production from semiconductor photocatalytic process has attracted much attention because this procedure uses the sufficient and renewable sunlight as the driving force. Moreover, the photocatalytic approach does not need to use H_2 and can be a safe and green method. In the past decades, the H_2O_2 production photocatalysts were mainly focused on TiO_2 and modified TiO_2 [14–16]. For example, Maurino et al. reported that surface fluorination of TiO_2 could lead to an increase in the production rate of H_2O_2 [14]. Tsukamoto et al. found that the surface deposition with Au-Ag alloy could improve the H_2O_2 production rate of TiO_2 [16]. Although TiO_2 or modified TiO_2 in the presence of oxygen can effectively produce H_2O_2 under UV light irradiation, H_2O_2 also suffer self-decomposition induced by UV light [17]. Furthermore, UV light accounts for only ~4% of sunlight [18]. Therefore, it is essential to

* Corresponding author.

E-mail addresses: donggh@ms.xjb.ac.cn (G. Dong), zengyubin@whu.edu.cn (Y. Zeng), cyywang@ms.xjb.ac.cn (C. Wang).



Scheme 1. (a) Schematic of g-C₃N₄; (b) carbon vacancy and amino group in g-C₃N₄.

design and develop visible light active photocatalysts which could efficiently produce H₂O₂ while inhibit the decomposition process.

Graphitic carbon nitride (g-C₃N₄) is a metal-free visible light photocatalyst very promising for hydrogen evolution because of its desirable band gap of 2.7 eV [19–21]. Since its conduction band potential (−1.3 V) is more negative than the reduction potential of O₂/H₂O₂ (0.695 V), g-C₃N₄ could reduce O₂ to H₂O₂ under visible light thermodynamically [22,23]. Shiraishi et al. found that H₂O₂ could be effectively produced by g-C₃N₄ in water/alcohol mixture under visible light irradiation [24]. However, in the absence of alcohol (organic scavenger), the efficacy of pure g-C₃N₄ was very low [25,26]. This is due to the fact that pure g-C₃N₄ has two disadvantages: (1) the fast recombination of photogenerated electrons and holes; (2) low chemical adsorption capability of O₂ on its surface [27–29]. According to previous reports, vacancy defects have been found to be able to trap photogenerated electrons thus inhibiting the recombination of photogenerated electrons and holes [30–32]. Meanwhile, vacancy defects can also enhance the adsorption and activation of gas molecular because of their abundant localized electrons [33,34]. In addition, amino nitrogen components can remarkably promote the interfacial electron transfer as recently observed by Zhang et al. [35]. Considering the advantages of vacancy and amino nitrogen, it is reasonable to hypothesize that the coexistence of vacancy defects and amino nitrogen may improve the H₂O₂ production activity of g-C₃N₄ in absence of organic scavenger. Coincidentally, the formation of carbon vacancies in the structure of g-C₃N₄ is accompanied by the appearance of amino group (Scheme 1). Therefore, it is of great interest to systematically study the correlation between carbon vacancy and H₂O₂ production performance of g-C₃N₄. However, to the best of our knowledge, limited work has been presented in this regard.

In this study, the effects of carbon vacancies on the oxygen reduction over g-C₃N₄ and the generation of H₂O₂ were systematically explored. Experimental results showed that carbon vacancy greatly improved the activity of g-C₃N₄ for H₂O₂ production in the absence of organic scavenger. A series of experiments were designed to identify the roles of carbon vacancies on the H₂O₂ production of g-C₃N₄ under visible light, and the mechanisms for the enhanced activity were analyzed in detail.

2. Experiments

2.1. Sample preparation

g-C₃N₄ was synthesized by following the protocol developed in our previous work [36]. Melamine (4 g) in a covered crucible (30 mL) was heated in static air with a ramp rate of 20 °C/min up to 520 °C where it was held for 4 h. Carbon vacancy contained g-C₃N₄ (Cv-g-C₃N₄) was synthesized by calcining the as-prepared g-C₃N₄ in a tube furnace at 520 °C under high purity argon gas flow for 2 h.

The resulted agglomerates were milled into powder in an agate mortar for further use.

2.2. Characterization

Power X-ray diffraction (XRD) patterns of the resulted samples were recorded on a Bruker D8 Advance diffractometer using Cu K α irradiation ($\lambda = 1.5418 \text{ \AA}$). Element analysis was performed on Vario MICRO. Fourier transform infrared (FT-IR) spectra were obtained on an FT-IR spectrophotometer (Nicolet iS50, Thermo) with KBr as the reference. Chemical compositions of the samples were analyzed using X-ray photoelectron spectroscopy (XPS) (VG Scientific ESCALAB Mark II spectrometer equipped with two ultrahigh vacuum chambers). All the binding energies were calibrated to the C 1s peak (284.6 eV) arising from the adventitious carbon. Electron spin resonance (ESR) signals were recorded on a Bruker ESR A300 spectrometer at room temperature (298 K). The Brunauer-Emmett-Teller surface areas of the samples were determined by nitrogen adsorption-desorption isotherm measurements at 77 K, using a Micrometrics ASAP2020 system after samples were vacuum-dried at 180 °C overnight. Optical absorption spectra were obtained using a UV-vis spectrometer (Shimadzu UV-2550). Photoluminescence spectra (PL) were measured on a fluorescence spectrometer (Hitachi F-4500) at 293 K.

2.3. Photocatalytic experiments

The photocatalytic activities of the samples were evaluated by the activation of molecular oxygen under visible light irradiation ($\lambda > 420 \text{ nm}$). A 300 W Xenon lamp with a 420 nm cutoff filter was chosen as visible light source. During each photocatalytic experiment, 0.1 g of a photocatalyst sample was dispersed into 100 mL of distilled water in a container with cooling water jacket outside. After that, the photocatalyst dispersion system was stirred in the dark for 2 h to ensure the adsorption-desorption equilibrium among the photocatalyst, dissolved oxygen and water before visible light irradiation. During the irradiation, about 4 mL of the suspensions was taken from the reaction cell at given time intervals, and then centrifuged to remove the photocatalyst particles. Subsequently, hydrogen peroxide (H₂O₂) was measured using a (p-hydroxyphenyl) acetic acid (POHPAA) analysis method [37]. Typically, a certain volume of fluorescence reagent (potassium hydrogen phthalate: 8.2 g/L, p-hydroxyphenylacetic acid: 270 mg/L, and type II horseradish peroxidase: 30 mg/L) was pre-added into the reaction system. 1.0 mL of sample was then withdrawn at an interval time of 2 h and then mixed with 1.0 mL of 1.0 mol/L NaOH for 10 min for measuring the intensity of the fluorescence emission at 409 nm excited at 315 nm.

Superoxide radicals ($\bullet\text{O}_2^-$) were examined by electron spin resonance (ESR) spectral measurement. ESR spectra of the radi-

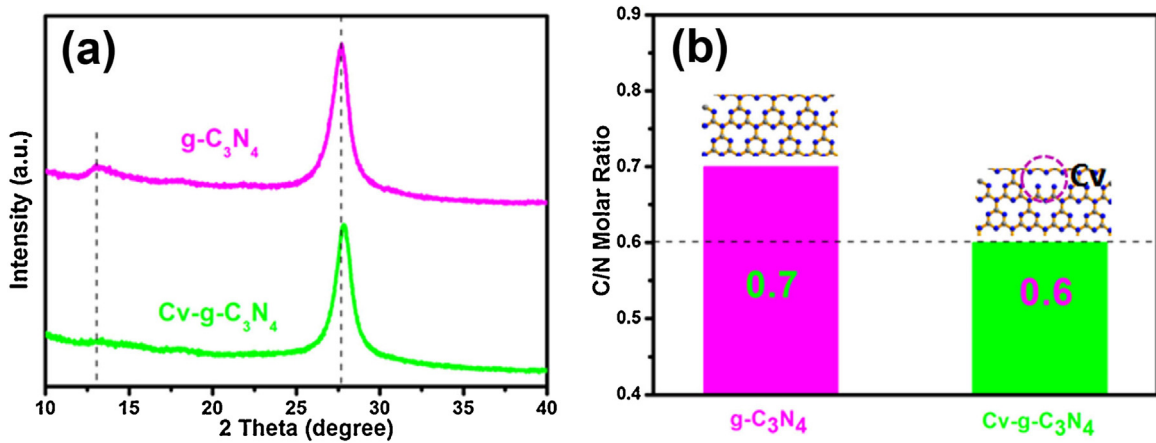


Fig. 1. (a) XRD patterns of $g\text{-C}_3\text{N}_4$ and $\text{Cv-g-C}_3\text{N}_4$; (b) C/N molar ratio in the $g\text{-C}_3\text{N}_4$ and $\text{Cv-g-C}_3\text{N}_4$.

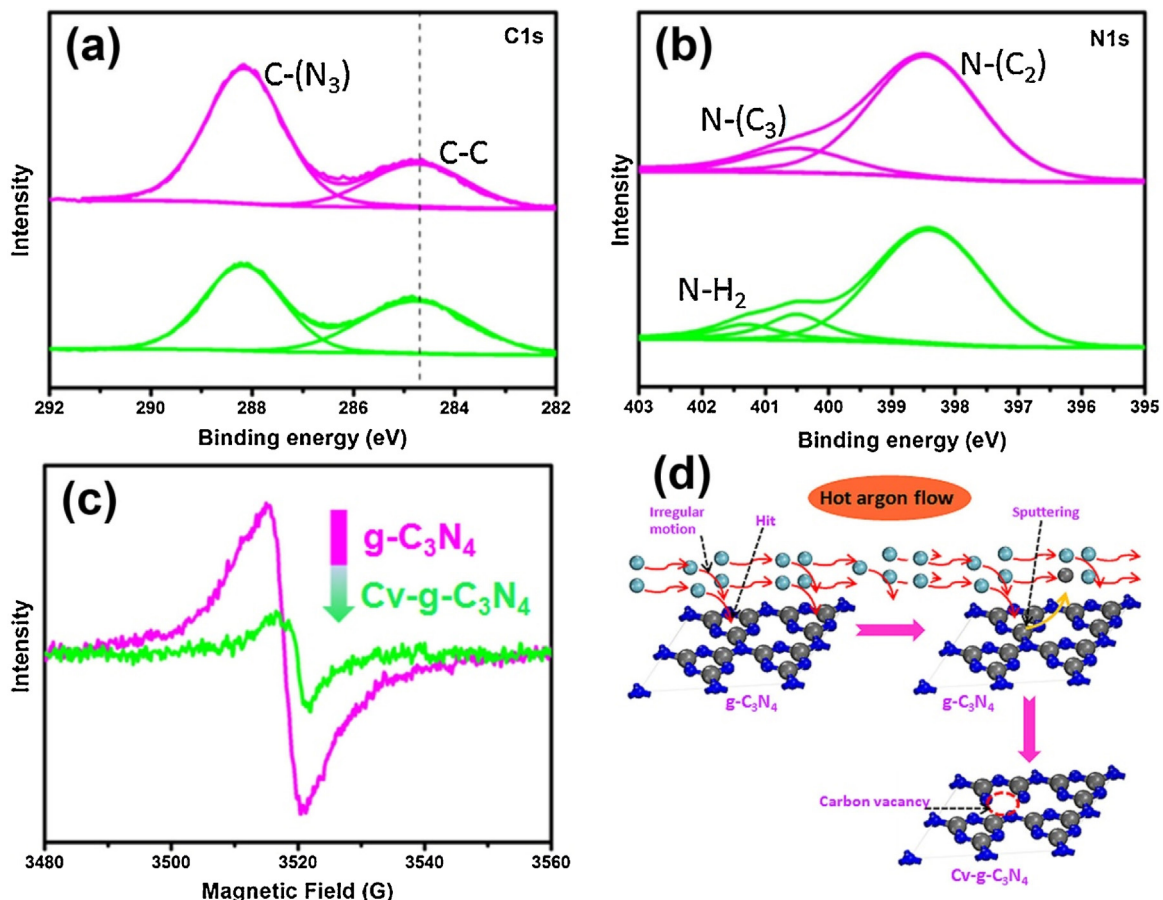


Fig. 2. (a) high-resolution XPS spectra of C 1s of $g\text{-C}_3\text{N}_4$ and $\text{Cv-g-C}_3\text{N}_4$; (b) high-resolution XPS spectra of N 1s of $g\text{-C}_3\text{N}_4$ and $\text{Cv-g-C}_3\text{N}_4$; (c) ESR spectra of $g\text{-C}_3\text{N}_4$ and $\text{Cv-g-C}_3\text{N}_4$; (d) possible formation mechanism of carbon vacancy.

cals were recorded on a Bruker EPR A300 spectrometer employing 5,5-dimethyl-l-pyrroline-N-oxide (DMPO) as the spin trapper. The spectra were collected with averages of 9 scans at 2 min after mixing the test sample in methanol solution. Methanol was used as the $\cdot\text{OH}$ radical scavenger to suppress the DMP $\text{O}-\text{OH}$ signal.

2.4. Theoretical calculations

The band structures and electron density calculations were carried out using the program package CASTEP, working in a plane

wave basis set. The Brillouin zones of the supercells were sampled by a grid of $3 \times 3 \times 1$ ($g\text{-C}_3\text{N}_4$ and $\text{Cv-g-C}_3\text{N}_4$) K-points. Electronic structures were calculated within the generalized gradient approximation from Perdew-Burke-Ernzerhof (GGA-PBE). The cut-off energy was 550 eV, and the Monkhorst-Pack k-point meshes were $5 \times 5 \times 3$ for all structures. In the process of calculation, the convergence tolerances were set as follows: $2.72\text{e-}5$ eV/atom for energy, 0.002 eV/ \AA for maximal force, 0.05 GPa for maximal stress, and 0.001 \AA for max.

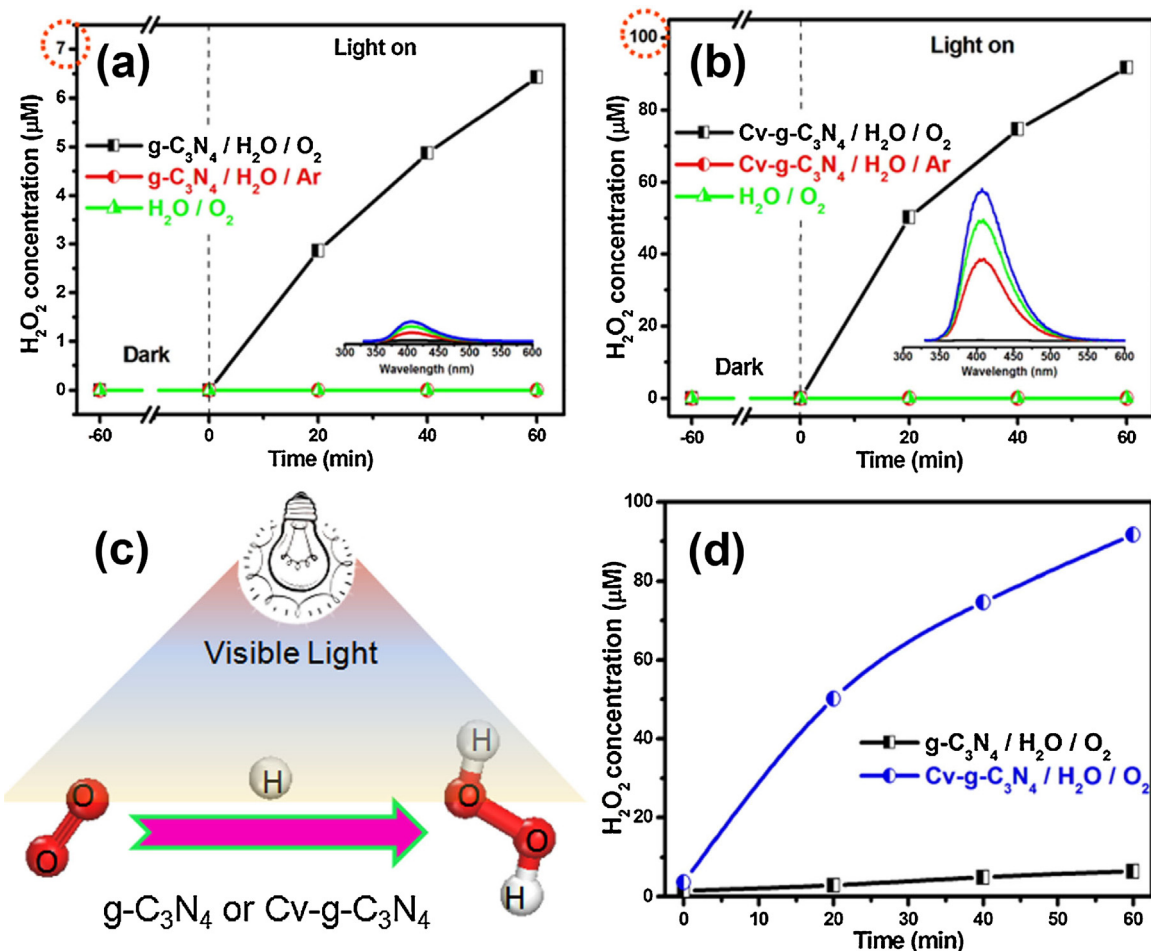


Fig. 3. (a) The concentration of generated H_2O_2 in different $\text{g-C}_3\text{N}_4$ systems; (b) the concentration of generated H_2O_2 in different $\text{Cv-g-C}_3\text{N}_4$ systems; (c) H_2O_2 production is accomplished by photocatalysis; (d) the concentration of H_2O_2 generated in $\text{g-C}_3\text{N}_4$ and $\text{Cv-g-C}_3\text{N}_4$ systems.

2.5. Photoelectrochemical experiments

Photoelectrochemical experiments were performed in a conventional three-electrode cell with a platinum plate ($1 \times 1 \text{ cm}^2$) as the auxiliary electrode and a saturated calomel electrode (SCE) as the reference electrode on a CHI 660C workstation. The photoelectrode (working electrode) was positioned in the middle of a 0.1 M KCl aqueous solution with the glass side facing the incident light. A 300 W Xe lamp with a 420 nm cutoff filter was chosen as a visible light source.

The photoelectrodes were prepared by a spin coating method. Typically, the aqueous slurries of $\text{g-C}_3\text{N}_4$ and $\text{Cv-g-C}_3\text{N}_4$ were spin-coated on ITO glass substrate at a spin rate of 3000 rpm for 30 s under low vacuum. The films on ITO glass substrate were dried in air and annealed at 200 °C for 1 h as final photoelectrodes.

3. Results and discussion

3.1. Structure characterization for samples

X-ray diffraction (XRD) is often used to characterize the phase structure of samples. As well known, $\text{g-C}_3\text{N}_4$ is featured with two XRD peaks: one at 13.0° corresponding to a d-spacing of 0.676 nm is arising from the in-plane structural packing motif, and the other at 27.4° is a characteristic interlayer stacking peak, corresponding to an interlayer distance of $d = 0.336 \text{ nm}$. As shown in Fig. 1a, both samples show a typical $\text{g-C}_3\text{N}_4$ structure without any impurity

phases, indicating that the heat treatment with argon gas did not affect the crystal structure of graphite-like carbon nitride. However, the peaks of $\text{Cv-g-C}_3\text{N}_4$ are weaker and shifted toward a higher 2θ value, suggesting that heat treatment with argon gas could destroy the crystallinity of $\text{g-C}_3\text{N}_4$ and could produce defects.

In order to identify the type of defects formed in the $\text{Cv-g-C}_3\text{N}_4$ framework, elemental analysis (EA) was used to determine the molar ratio of carbon to nitrogen (C/N) in the products. The C/N molar ratio of $\text{Cv-g-C}_3\text{N}_4$ is 0.6 (Fig. 1b), lower than that of $\text{g-C}_3\text{N}_4$ (0.7). This indicates that the defects formed in the $\text{Cv-g-C}_3\text{N}_4$ framework are carbon vacancies. Additionally, the content of H element in $\text{Cv-g-C}_3\text{N}_4$ is very plentiful, suggesting that more amino groups ($-\text{NH}_2$) were generated in $\text{Cv-g-C}_3\text{N}_4$ after the heat treatment with argon gas.

X-ray photoelectron spectroscopy (XPS) was further used to investigate the chemical compositions of the carbon nitride samples (Fig. 2a and b). High-resolution XPS peaks of C 1s of the two samples can be fitted with two peaks at binding energies of 288.2 and 284.6 eV, which are ascribed to the tertiary carbon C—N₃ and C—C (arising from the adventitious carbon) groups, respectively. The area ratios of the two peaks at 288.2 and 284.6 eV were calculated to be 2.7 and 1.2 for $\text{g-C}_3\text{N}_4$ and $\text{Cv-g-C}_3\text{N}_4$, respectively. The decrease of tertiary carbon content percentage supports the assumption of carbon vacancy formation. In addition, the high-resolution XPS peaks of N 1s of $\text{g-C}_3\text{N}_4$ can be fitted with two peaks centered at 398.4 and 400.7 eV, which are ascribed to the tertiary carbon C—N—C and C—N₃ (arising from the adventitious carbon)

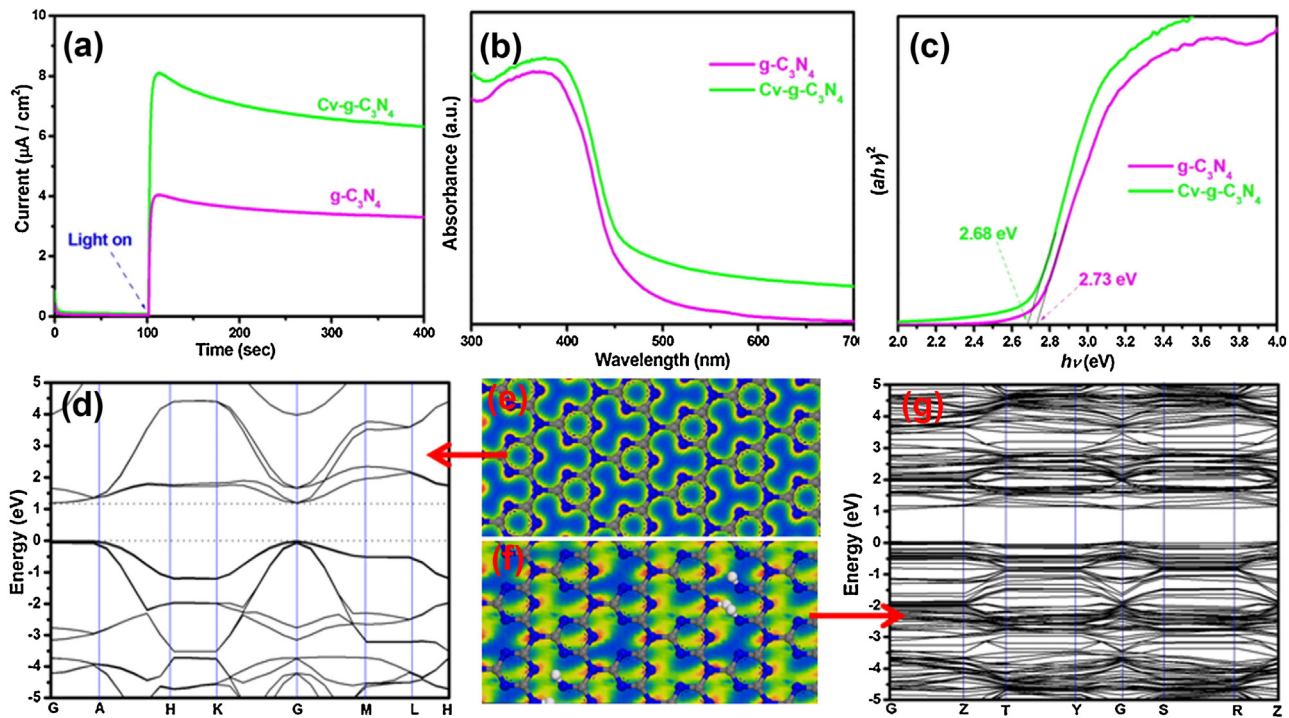


Fig. 4. (a) The photocurrent generated on $\text{g-C}_3\text{N}_4$ and $\text{Cv-g-C}_3\text{N}_4$; (b) UV-vis diffuse reflectance spectra of $\text{g-C}_3\text{N}_4$ and $\text{Cv-g-C}_3\text{N}_4$; (c) plots of $(ahv)^2$ vs. the energy of absorbed light of $\text{g-C}_3\text{N}_4$ and $\text{Cv-g-C}_3\text{N}_4$; (d) calculated band structure of $\text{g-C}_3\text{N}_4$; (e) calculated electron density of $\text{g-C}_3\text{N}_4$; (f) calculated electron density of $\text{Cv-g-C}_3\text{N}_4$; (g) calculated band structure of $\text{g-C}_3\text{N}_4$.

groups, respectively. However, in addition to the N 1s peaks at 398.4 and 400.7 eV, a new peak at higher binding energy of 401.3 eV appeared in the high-resolution XPS spectra of $\text{Cv-g-C}_3\text{N}_4$ (Fig. 2b). This peak is attributed to the amino groups ($-\text{NH}_2$) formed by the disappearance of tertiary carbon and further supports the formation of carbon vacancies.

Besides EA and XPS, Electron spin resonance (ESR) was also employed to verify the formation of carbon vacancies. Fig. 2c shows that $\text{g-C}_3\text{N}_4$ exhibits a Lorentzian line centered at about 3512 G, which is arisen from the unpaired electrons on the carbon atoms of the aromatic rings. Compare with pure $\text{g-C}_3\text{N}_4$, $\text{Cv-g-C}_3\text{N}_4$ possesses a much weaker ESR signal, suggesting the decrease of carbon content in $\text{Cv-g-C}_3\text{N}_4$. Therefore, it is concluded that carbon vacancies have been successfully formed in $\text{g-C}_3\text{N}_4$ after the heat treatment with argon gas.

Since surface and bulk defects play different roles in photocatalytic processes, it is crucial to identify the positions of carbon vacancies in the $\text{Cv-g-C}_3\text{N}_4$. In this prospect, high-resolution XPS depth profiles analysis was employed to monitor the $-\text{NH}_2$ change in the $\text{Cv-g-C}_3\text{N}_4$. It is found that the peak intensity of $-\text{NH}_2$ decreases continuously upon the etching time from 0 to 240 s, indicating the carbon vacancies mainly exist on the surface of $\text{Cv-g-C}_3\text{N}_4$ (Fig. S1, in Supporting information). Fig. 2d shows the possible formation mechanism of carbon vacancy. In the procedure of calcination, high temperature give the enormous energy to argon molecules. This makes a part of argon molecules do the irregular motion. Molecules which do irregular motion may hit the surface atoms. When argon molecule hit surface atom, it will impart energy to the targeted atom. If the imparted energy exceeds the binding energy of the targeted atom, targeted atom can be sputtered from the surface and form a vacancy simultaneously. As we know, carbon atom has a bigger surface area and smaller molecular weight than nitrogen atom. The bigger surface area makes carbon atom to accept more energy. Meanwhile, the smaller molecular weight and

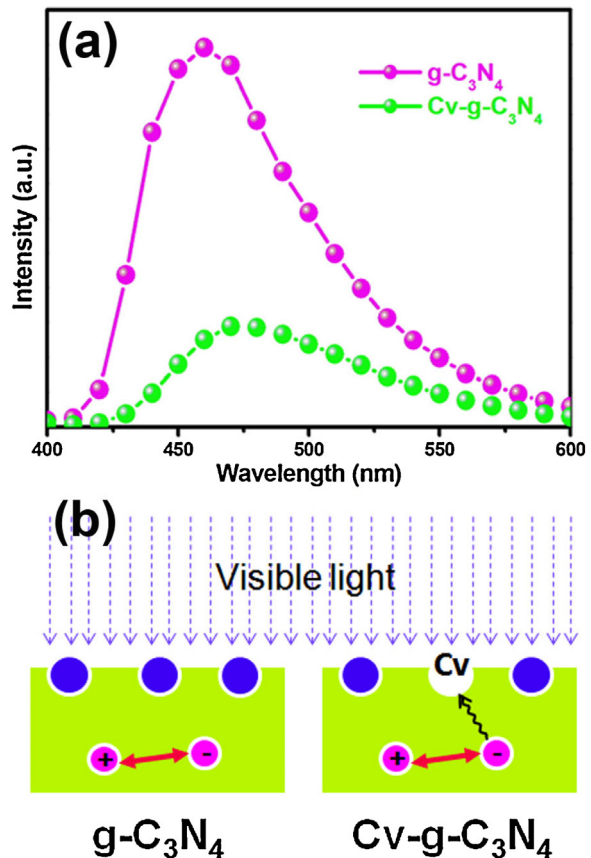


Fig. 5. (a) photoluminescence (PL) spectra of $\text{g-C}_3\text{N}_4$ and $\text{Cv-g-C}_3\text{N}_4$; (b) carbon vacancy could significantly inhibit the recombination of photogenerated carriers.

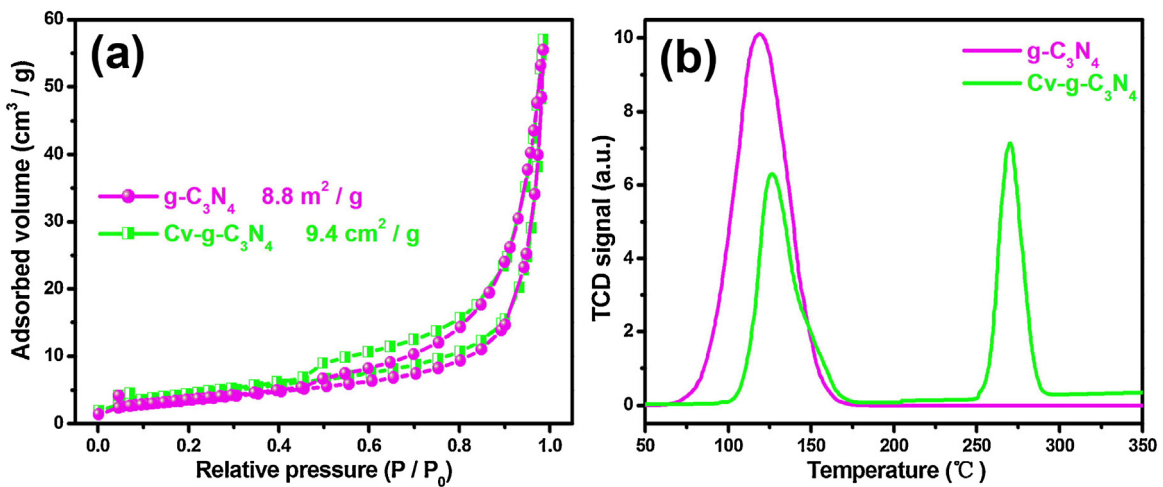


Fig. 6. (a) N_2 adsorption-desorption isotherms of $g\text{-}C_3N_4$ and $\text{Cv}\text{-}g\text{-}C_3N_4$; (b) TPD spectra of $g\text{-}C_3N_4$ and $\text{Cv}\text{-}g\text{-}C_3N_4$.

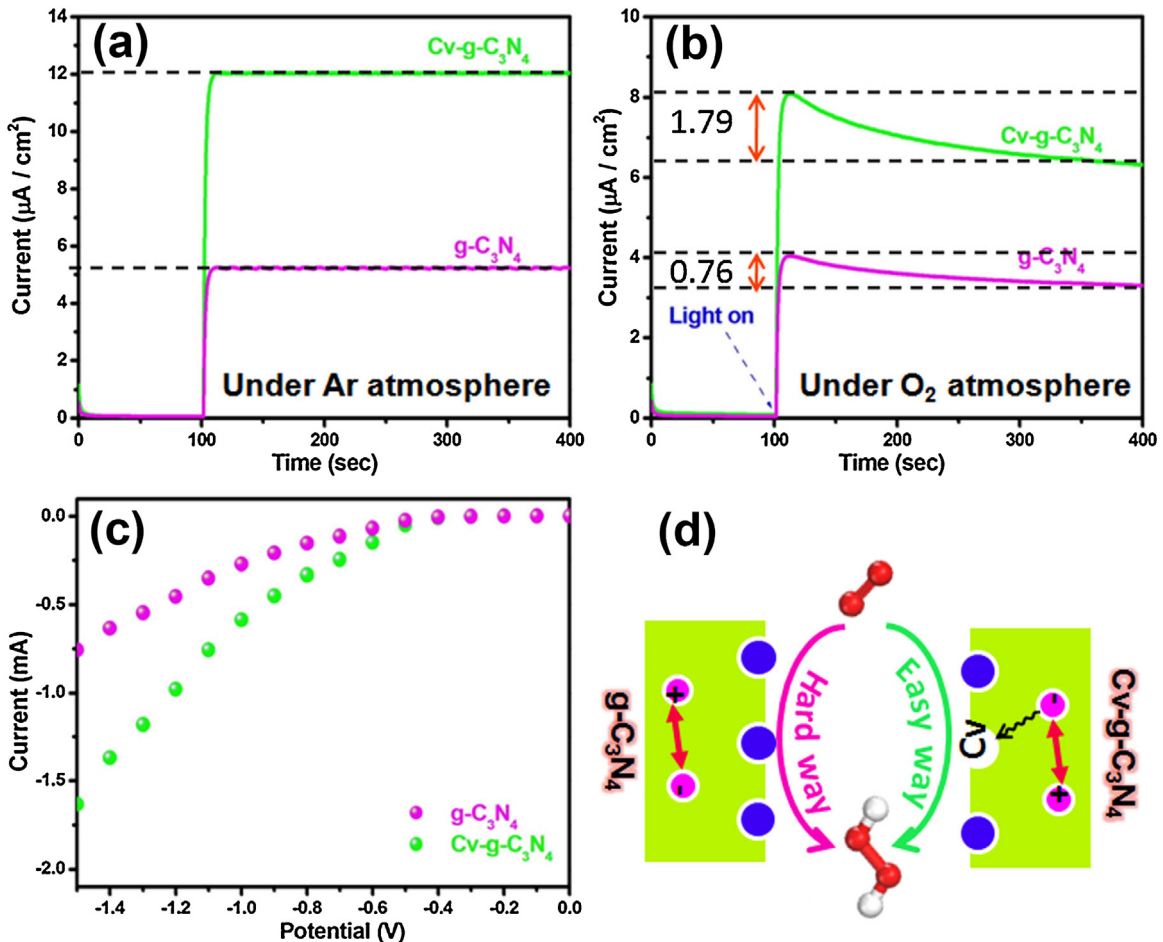


Fig. 7. (a) Photocurrent decay measurements were conducted under Ar atmosphere; (b) photocurrent decay measurements were conducted under O_2 atmosphere; (c) linear sweep voltammetry (LSV) curves of $g\text{-}C_3N_4$ and $\text{Cv}\text{-}g\text{-}C_3N_4$; (d) carbon vacancy makes the molecular oxygen reduction on $\text{Cv}\text{-}g\text{-}C_3N_4$ easier than that on $g\text{-}C_3N_4$.

the bigger energy make carbon atom more likely to be sputtered from the surface.

3.2. Photocatalytic H_2O_2 production

H_2O_2 can be produced in both $g\text{-}C_3N_4$ and $\text{Cv}\text{-}g\text{-}C_3N_4$ systems (Fig. 3). Control experiments show that H_2O_2 cannot be detected when oxygen is eliminated by argon gas, indicating oxygen is essen-

tial for the generation of H_2O_2 (Fig. 3a). That means O_2 could be effectively reduced to H_2O_2 in the presence of water over both $g\text{-}C_3N_4$ and $\text{Cv}\text{-}g\text{-}C_3N_4$. However, in the absence of either photocatalyst or visible light, there is no H_2O_2 production (Fig. 3a). This result unambiguously illustrates that the process of H_2O_2 production is accomplished by photocatalysis (Fig. 3c). As shown in Fig. 3a and d, the H_2O_2 production in $g\text{-}C_3N_4$ suspension slowly increases with extending the reaction time. Interestingly, the yield of pro-

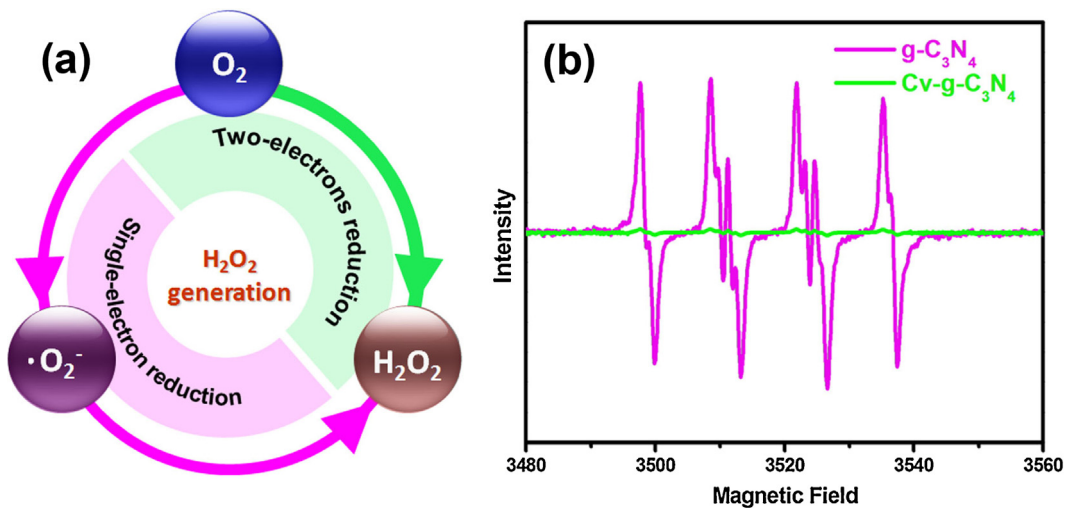


Fig. 8. (a) The possible generation routes of H_2O_2 ; (b) 5,5-dimethyl-pyrroline N-oxide (DMPO) spin trapping ESR technique to measure $\cdot\text{O}_2^-$ generated during the generation of H_2O_2 .

duced H_2O_2 over $\text{Cv-g-C}_3\text{N}_4$ in the same visible light irradiation time is much higher than that over $\text{g-C}_3\text{N}_4$ (Fig. 3b and d). Obviously, $\text{Cv-g-C}_3\text{N}_4$ is more active for the photoreduction of O_2 to H_2O_2 , namely, 14 times more activity than $\text{g-C}_3\text{N}_4$. The influence of initial pH values on the H_2O_2 generation in the $\text{Cv-g-C}_3\text{N}_4/\text{H}_2\text{O}/\text{O}_2$ system was also investigated. We found that the pH value variation in the range of 5.0–7.0 did not affect the H_2O_2 production (Fig. S2, in Supporting information), suggesting that $\text{Cv-g-C}_3\text{N}_4$ can efficiently produce H_2O_2 in a wide working pH range.

Niu et al. revealed that nitrogen vacancy could also improve the photocatalytic activity of $\text{g-C}_3\text{N}_4$ [38]. To compare the improve effect of carbon vacancy and nitrogen vacancy, we synthesized the $\text{g-C}_3\text{N}_4$ with nitrogen vacancies ($\text{Nv-g-C}_3\text{N}_4$). The synthesis procedure of $\text{Nv-g-C}_3\text{N}_4$ was similar to that of $\text{Cv-g-C}_3\text{N}_4$ but changed the argon gas to hydrogen gas. The activity comparison in Fig. S3 (in Supporting information) suggests that the activity of $\text{Cv-g-C}_3\text{N}_4$ is 6 times of that of $\text{Nv-g-C}_3\text{N}_4$. This result suggests that carbon vacancy is more effective for photocatalytic H_2O_2 generation than nitrogen vacancy.

3.3. The mechanism of activity enhancement

Since the production of H_2O_2 needs photogenerated electrons to reduce O_2 , the generation of H_2O_2 relies on the amount of photogenerated electrons. As is well known, photocurrent also depends on the amount of photoelectrons transferred from semiconductor to the ITO glass substrate. The higher the photocurrent is, the more the photoelectrons are produced. Fig. 4a shows that the photocurrent (The applied bias is 0 V vs SCE) generated over $\text{Cv-g-C}_3\text{N}_4$ reaches $8.12 \mu\text{A cm}^{-2}$, 2.0 times that of $\text{g-C}_3\text{N}_4$ ($4.05 \mu\text{A cm}^{-2}$). The higher photocurrent in $\text{Cv-g-C}_3\text{N}_4$ implies that it could produce more photoelectrons to reduce O_2 molecule compared to $\text{g-C}_3\text{N}_4$.

Generally, the production of photoelectrons relates to three processes: visible light absorption, photoexcitation, and the separation of photoinduced charge carriers. UV-vis absorption spectra of $\text{g-C}_3\text{N}_4$ and $\text{Cv-g-C}_3\text{N}_4$ show the difference in absorption edges of the two samples. As seen in Fig. 4b, the intrinsic absorption edge of $\text{Cv-g-C}_3\text{N}_4$ shows a red shift compared with that of $\text{g-C}_3\text{N}_4$. In addition, the absorption spectrum of $\text{Cv-g-C}_3\text{N}_4$ extends to the whole visible light region, even in the infrared region, thereby enhancing the absorption of light. This is consistent with the previous reports that vacancy defects can increase the visible light absorption of photo-

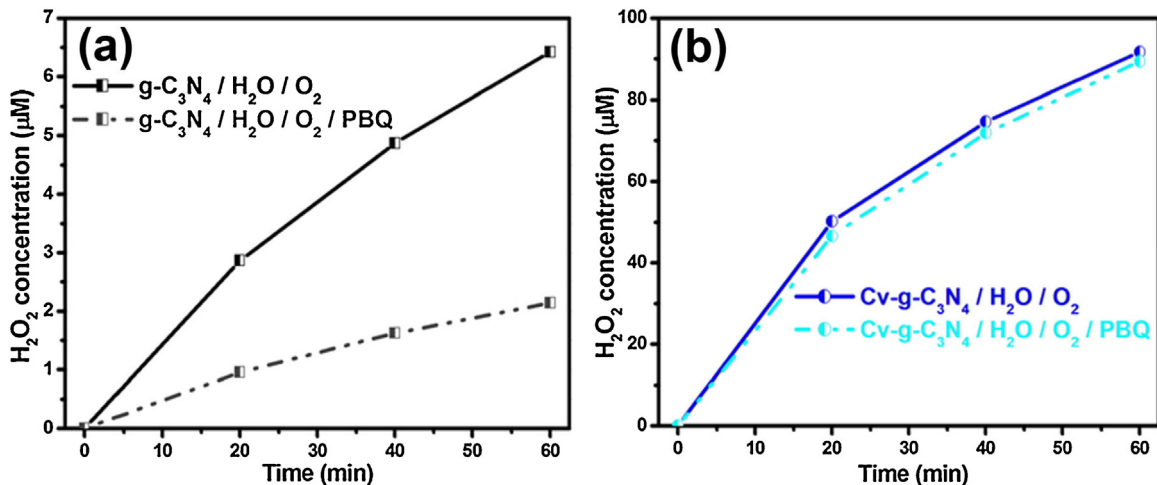


Fig. 9. (a) The influence of p -benzoquinone (PBQ, 1 mM, $\cdot\text{O}_2^-$ scavenger) for the H_2O_2 generation on $\text{g-C}_3\text{N}_4$; (b) the influence of p -benzoquinone (PBQ, 1 mM, $\cdot\text{O}_2^-$ scavenger) for the H_2O_2 generation on $\text{Cv-g-C}_3\text{N}_4$.

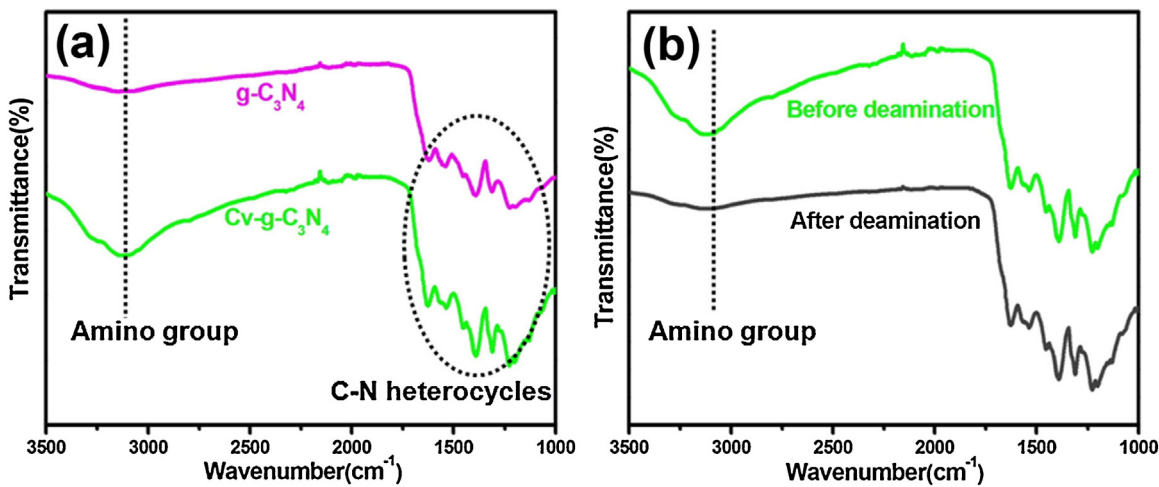


Fig. 10. (a) FT-IR spectra of $g\text{-C}_3\text{N}_4$ and $\text{Cv-g-C}_3\text{N}_4$ samples; (b) FT-IR spectra of $\text{Cv-g-C}_3\text{N}_4$ before and after the deamination.

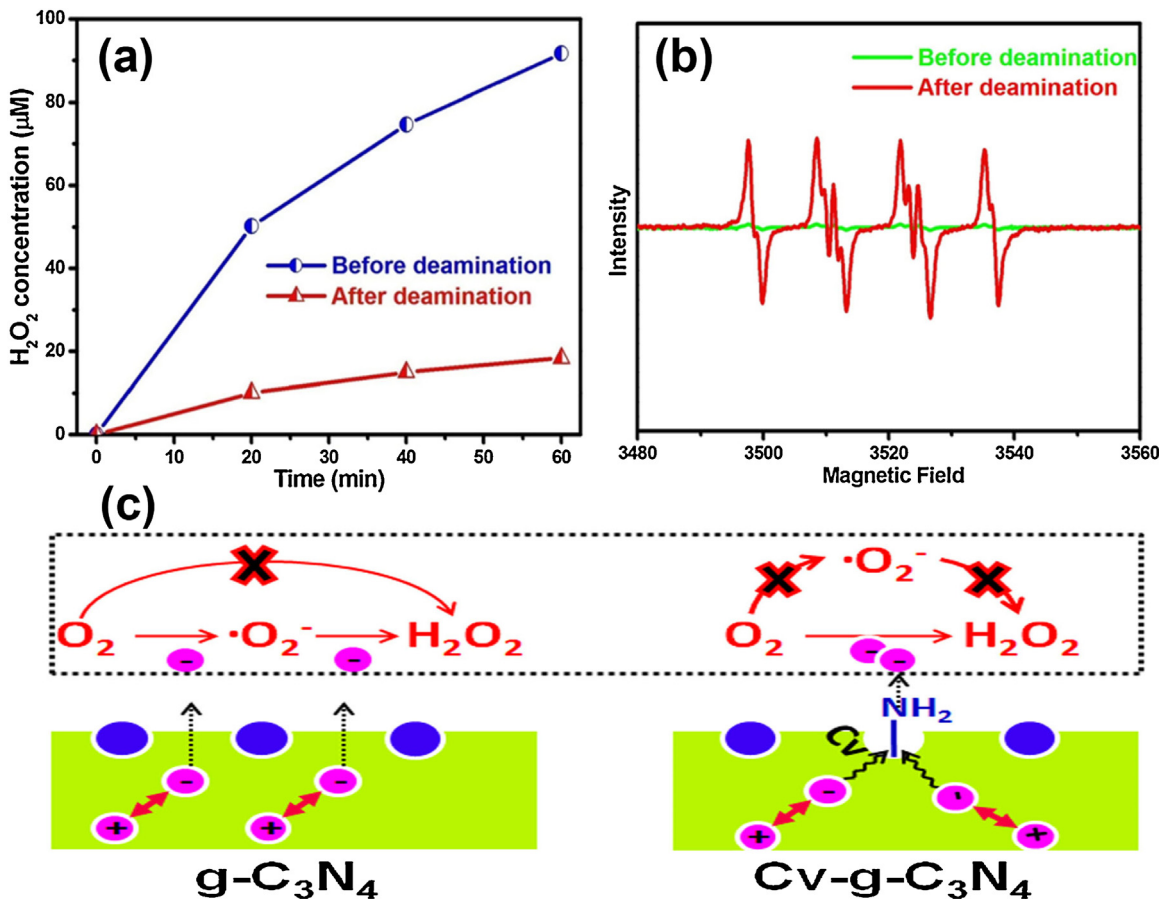


Fig. 11. (a) The influence of deamination for the H_2O_2 generation on $\text{Cv-g-C}_3\text{N}_4$; (b) the influence of deamination for the $\cdot\text{O}_2^-$ generation; (c) amino group changed the H_2O_2 generation pathway from single-electron reduction to two-electron reduction.

catalysts [33]. From the absorption spectra and simulation results (Fig. 4d and g, both $g\text{-C}_3\text{N}_4$ and $\text{Cv-g-C}_3\text{N}_4$ are direct-gap semiconductors), the corresponding band gaps of $g\text{-C}_3\text{N}_4$ and $\text{Cv-g-C}_3\text{N}_4$ can be derived as 2.73 and 2.68 eV respectively (Fig. 4c), indicating that carbon vacancy could narrow the band gap of $g\text{-C}_3\text{N}_4$. Thus, the excitation of valence band electrons in $\text{Cv-g-C}_3\text{N}_4$ will be much easier than that in $g\text{-C}_3\text{N}_4$. In order to determine the position of the conduction band and the valence band of $g\text{-C}_3\text{N}_4$ and $\text{Cv-g-C}_3\text{N}_4$,

Mott–Schottky measurements were performed. As shown in Fig. S4 (in Supporting information), both of the two samples displayed n-type semiconductor characteristic. The flat-band potentials of both $g\text{-C}_3\text{N}_4$ and $\text{Cv-g-C}_3\text{N}_4$ is estimated to be about -1.29 eV versus SCE. For n-type semiconductor, the conduction band position is very close to their flat-band potential. Therefore, the conduction band potentials of both $g\text{-C}_3\text{N}_4$ and $\text{Cv-g-C}_3\text{N}_4$ is -1.29 eV versus SCE, which more negative than the redox potential of $\text{O}_2/\text{H}_2\text{O}_2$ (0.695 V).

The VB potentials are calculated to be 1.44 and 1.39 eV for g-C₃N₄ and Cv-g-C₃N₄ by using the formula Eg = Ev – Ec (Eg: band gap, Ev: VB potential, Ec: CB potential). This up shift of VB potential may be caused by the valence band broadening which could be attributed to the carbon vacancy.

To further understand the change of the band structure induced by carbon vacancies, the band structures and the electron densities of g-C₃N₄ and Cv-g-C₃N₄ were simulated via the plane-wave-pseudopotential approach based on the density functional theory. From Fig. 4d and g, it can be seen that the carbon vacancies could narrow the band gap of g-C₃N₄ to enhance its visible light absorption. Meanwhile, the energy level density of valence band of Cv-g-C₃N₄ is much higher than that of g-C₃N₄, revealing that carbon vacancies make Cv-g-C₃N₄ instead of g-C₃N₄ possess more excitable electrons. This is understandable after considering that carbon vacancies reduced the symmetry of g-C₃N₄ and produced the effect of electron delocalization. The symmetry reduction and electron delocalization are shown in the electron density maps (Fig. 4e and f).

Photoluminescence (PL) spectra were used to explore the recombination and separation of photogenerated electrons and holes in the g-C₃N₄ and Cv-g-C₃N₄ samples (Fig. 5a). The emission peak appearing at about 455 nm is attributed to the direct electron-hole recombination of band transition. Compare with pure g-C₃N₄, Cv-g-C₃N₄ possess a much weaker emission peak, implying that the separation efficiency of photogenerated carriers is improved by carbon vacancies. The reason of increased separation efficiency can be explained by electrical conductivity. Electrochemical impedance spectroscopy (EIS) was employed to study the electrical conductivity of the resulting samples. Fig. S5 (in Supporting information) reveals that the Nyquist plots diameter of Cv-g-C₃N₄ is much smaller than that of g-C₃N₄, confirming that the carbon vacancies could increase the electrical conductivity. Carbon vacancies originate from the breaking of the covalent bonds between carbon and nitrogen atoms, accompanied by many unsaturated N atoms. These unsaturated N atoms could act as the paramagnetic centers and attract photoelectrons from the conduction band of Cv-g-C₃N₄ (Fig. 5b). Therefore, carbon vacancies could significantly inhibit the recombination of photogenerated carriers, thus increasing the yield of photoelectrons.

Based on the experimental observations in conjunction with theoretical calculation, the fact that Cv-g-C₃N₄ could produce more photoelectrons can be attributed to the following. First, carbon vacancies made Cv-g-C₃N₄ to hold more excitable electrons; second, carbon vacancies could narrow the band gap of g-C₃N₄ to enhance its visible light absorption; and third, carbon vacancies could significantly inhibit the recombination of photogenerated carriers.

Besides the amount of photogenerated electrons, the H₂O₂ production performance may also depend on the adsorption capacity and adsorption strength of molecular oxygen onto the surface of g-C₃N₄ because the photocatalytic process is surface related. In general, adsorption capacity is proportional to the surface area of a sample. The surface areas of g-C₃N₄ and Cv-g-C₃N₄ were analyzed through nitrogen adsorption-desorption isotherms. Fig. 6a shows that the Brunauer–Emmett–Teller specific surface areas of g-C₃N₄ and Cv-g-C₃N₄ are 8.8 and 9.4 m²/g, respectively, indicating that the adsorption amount of molecular oxygen on Cv-g-C₃N₄ is approximate to that on g-C₃N₄.

For adsorption strength, it is strongly dependent on the interaction between surface sites and adsorbates, thereby classified into different adsorption types including physisorption and chemisorption. Temperature-programmed desorption (TPD) investigations were carried out to study the adsorption type and adsorption strength of molecular oxygen on the surface of two samples. As

shown in Fig. 6b (detailed experiments can be found in Supporting information), there are two types of O₂ adsorbed species present on Cv-g-C₃N₄ compared to only one on g-C₃N₄. The peak at about 120 °C relates to physical adsorption. This peak from Cv-g-C₃N₄ is much weaker than that from g-C₃N₄. Moreover, the peak at 270 °C, corresponding to the strong chemisorption species of O₂, could be observed for Cv-g-C₃N₄ but not for g-C₃N₄. These observations suggest that, although the amount of molecular oxygen adsorbed on g-C₃N₄ and Cv-g-C₃N₄ is comparable, the adsorption strength of molecular oxygen on Cv-g-C₃N₄ is stronger than that on g-C₃N₄. According to previous reports, the oxygen atom of O₂ has a single electron, making the gas behave as a Lewis acid. Meanwhile, the N atom of amino group around carbon vacancy acts as a Lewis base. These behaviors indicate that O₂ can interact with the N atom of amino group via Lewis acid–base interactions. Therefore, the chemisorption of O₂ over Cv-g-C₃N₄ involves the O atom of O₂ bonding with the N atom of amino group around the carbon vacancy. The stronger the adsorption is, the easier the electrons transfer [34].

In order to explore the correlation between adsorption and electron transfer directly, photocurrent decay measurements were conducted. Under Ar atmosphere, the photocurrent generated on both g-C₃N₄ and Cv-g-C₃N₄ electrode is stabilized with irradiation time during the entire irradiation period (Fig. 7a). However, the photocurrent of both g-C₃N₄ and Cv-g-C₃N₄ gradually decay under O₂ atmosphere (Fig. 7b). Moreover, the photocurrent decay of g-C₃N₄ is much slower than that of Cv-g-C₃N₄. Since photocurrent decay mainly occurs due to the competition between O₂ and ITO glass for trapped electrons [34], it is concluded that carbon vacancies help the photogenerated electrons to transfer from g-C₃N₄ to the adsorbed O₂.

Chemical adsorption sites are often regarded as reaction centers capable of activating adsorbate [33,34]. Activation generally refers to the process whereby adsorbate is excited for a subsequent reaction. Therefore, it will be easier to reduce molecular oxygen on Cv-g-C₃N₄ than on g-C₃N₄. To test this hypothesis, linear sweep voltammetry (LSV) was carried out to investigate the reduction of oxygen. Fig. 7c shows the ORR catalytic performance for g-C₃N₄ and Cv-g-C₃N₄ under the LSV test. Compare with the LSV curve of g-C₃N₄, cathodic current is enhanced greatly on Cv-g-C₃N₄. This observation proves that carbon vacancies make the molecular oxygen reduction on Cv-g-C₃N₄ easier than that on g-C₃N₄ (Fig. 7d).

Hydrogen peroxide might be generated through either a sequential two-step single-electron indirect reduction (O₂ → •O₂[–] → H₂O₂) or an one-step two-electron direct reduction (O₂ → H₂O₂) route (Fig. 8a). To clarify the mechanisms of photocatalytic H₂O₂ production on g-C₃N₄ and Cv-g-C₃N₄, DMPO spin-trapping ESR technique was employed to measure the •O₂[–] in photocatalysis (Fig. 8b). Four characteristic peaks of DMPO-•O₂[–] are clearly observed in methanolic suspensions of g-C₃N₄, while no peak could be found in methanolic suspension of Cv-g-C₃N₄. The significant difference in DMPO-•O₂[–] signals strongly implies that carbon vacancies change the transfer pathway of photoelectrons. Although Cv-g-C₃N₄ could not produce •O₂[–], it could generate H₂O₂ directly under the visible light irradiation. Based on these observations, we speculate that H₂O₂ in g-C₃N₄ suspension is achieved through a two-step single-electron indirect reduction pathway (e[–] → •O₂[–] → H₂O₂); while in Cv-g-C₃N₄ suspension, it is achieved through one-step two-electron direct reduction pathway (e[–] → H₂O₂). To confirm this speculation, active species trapping experiments were further carried out. As shown in Fig. 9a and b, the addition of *p*-benzoquinone (PBQ, 1 mM, •O₂[–] scavenger) does not change the H₂O₂ generation on Cv-g-C₃N₄ while it could actually depress the H₂O₂ generation on g-C₃N₄. This unambiguously proves that carbon vacancies change the H₂O₂ generation pathway

over $\text{g-C}_3\text{N}_4$ under visible light from a two-step single-electron indirect reduction to an one-step two-electron direct reduction.

The one-step two-electron pathway of H_2O_2 production was further confirmed by the rotating disc electrode (RDE) experiment. For pristine $\text{g-C}_3\text{N}_4$, the typical two-step pathway at around -0.5 V and -1.2 V is observed, indicating a successive single-electron reduction (Fig. S6, in Supporting information). Interestingly, when $\text{g-C}_3\text{N}_4$ is replaced by $\text{Cv-g-C}_3\text{N}_4$, the first reduction plateau vanished. The LSV curves show a single-step plateau, indicating an one-step two-electron direct reduction pathway.

Zhang and his coworkers have investigated the effects of various nitrogen species in ORR process [35]. They observed that electron transfer number depends on the amino nitrogen components in metal-free catalysts. In our system, carbon vacancies are surrounded by many N-dangling bands (unsaturated N atoms). Dangling bonds of N atoms are compensated by adsorbed hydrogen and form many amino groups. The formation of amino group on $\text{Cv-g-C}_3\text{N}_4$ is confirmed by FTIR measurements (Fig. 10a). Therefore, the one-step two-electron reduction pathway could be attributed to amino groups around carbon vacancies. To clarify this point, it is necessary to remove amino groups from $\text{Cv-g-C}_3\text{N}_4$ and then compare the H_2O_2 production performance before and after deamination. In this work, a simple and common chemical deamination approach was designed to remove the amino groups from $\text{Cv-g-C}_3\text{N}_4$ (Detailed experiments can be found in Supporting information). As seen from Fig. 10b that, after deamination, the absorption band of amino group is significantly decreased. This result suggests that amino groups are effectively removed in deamination approach. Furthermore, H_2O_2 and $\bullet\text{O}_2^-$ measurements were carried out to evaluate the contribution of amino group to H_2O_2 production. As shown in Fig. 11a, the deamination could greatly inhibit the generation of H_2O_2 in $\text{Cv-g-C}_3\text{N}_4$, while the ratio of maximum concentration of hydrogen peroxide after the deamination is only about 19.9% of that before the deamination. Moreover, it is very interesting to notice that deamidated $\text{Cv-g-C}_3\text{N}_4$ in methanol dispersion gives stronger ESR signals of DMPO- $\bullet\text{O}_2^-$ (Fig. 11b). However, these generated superoxide radicals could not be produced before deamination, confirming that one-step two-electron direct reduction pathway is attributed to amino groups around carbon vacancies.

The stability of the $\text{Cv-g-C}_3\text{N}_4$ during the photocatalytic H_2O_2 production was evaluated by recycling test (Fig. S7, in Supporting Information). No significant change in the photocatalytic activity occurs after four cycles, indicating that $\text{Cv-g-C}_3\text{N}_4$ is stable during the photocatalytic H_2O_2 production.

4. Conclusions

In summary, we have demonstrated that carbon vacancies could be introduced on the surface of $\text{g-C}_3\text{N}_4$ by simple calcinations with argon gas. The carbon vacancies modified $\text{g-C}_3\text{N}_4$ could efficiently reduce atmospheric O_2 to H_2O_2 under visible light, without using any precious metal cocatalysts or organic scavengers. The presence of carbon vacancies could reduce the symmetry of $\text{g-C}_3\text{N}_4$ and narrow down its band gap, thus extending the visible light absorption and increasing the excitable electrons. Moreover, carbon vacancies could activate O_2 and change the H_2O_2 generation pathway from a two-step single-electron indirect reduction to a one-step two-electron direct reduction. This study not only provides a new strategy to improve the photocatalytic H_2O_2 production, but also underlines the significance of the correlation between the surface defect structure and the activity of semiconductor photocatalysts.

Acknowledgments

This work was supported by National Science Foundation of China (Grants 21473248), scientific research start-up funds for postdoctor (Y55P411601), the "Western Light" Program of Chinese Academy of Sciences (2015-XBQN-B-06) and the CAS/SAFEA International Partnership Program for Creative Research Teams. We gratefully acknowledge Dr Tao Pang (AQNU, China) for valuable discussions and Prof. Y. S. Chai for language polish.

Appendix A. Supplementary data

Supplementary data associated with this article can be found, in the online version, at <http://dx.doi.org/10.1016/j.apcatb.2016.03.004>.

References

- [1] J.M. Campos-Martin, G. Blanco-Brieva, J.L. Fierro, *Angew. Chem. Int. Ed.* **45** (2006) 6962–6984.
- [2] J.J. Peng, F. Shi, Y.L. Gu, Y.Q. Deng, *Green Chem.* **5** (2003) 224–226.
- [3] S. Niwa, M. Eswaramoorthy, J. Nair, A. Raj, N. Itoh, H. Shoji, T. Namba, F. Mizukami, *Science* **295** (2002) 105–107.
- [4] Z.H. Ai, L.R. Lu, J.P. Li, L.Z. Zhang, J.R. Qiu, M.H. Wu, *J. Phys. Chem. C* **117** (2007) 4087–4093.
- [5] Y.J. Cui, Z.X. Ding, P. Liu, M. Antouietti, X.Z. Fu, X.C. Wang, *Phys. Chem. Chem. Phys.* **14** (2012) 1455–1462.
- [6] Y.X. Qin, F.H. Song, Z.H. Ai, P.P. Zhang, L.Z. Zhang, *Environ. Sci. Technol.* **49** (2015) 7948–7956.
- [7] R. Hage, A. Lienk, *Angew. Chem. Int. Ed.* **45** (2006) 206–222.
- [8] C. Prat, M. Vicente, S. Esplugas, *Water Res.* **22** (1988) 663–668.
- [9] M. Perez, F. Torrades, X. Domenech, J. Peral, *Water Res.* **36** (2002) 2703–2710.
- [10] X.F. Chen, J.S. Zhang, X.Z. Fu, M. Antonietti, X.C. Wang, *J. Am. Chem. Soc.* **131** (2009) 11658–11659.
- [11] V.R. Choudhary, A.G. Gaikwad, S.D. Sansare, *Angew. Chem. Int. Ed.* **40** (2001) 1776–1779.
- [12] P. Landon, P.J. Collier, A.J. Papworth, C.J. Kiely, G.J. Hutchings, *Chem. Commun.* **205** (2002) 8–2059.
- [13] T.P. Fellingar, F. Hasché, P. Strasser, M. Antonietti, *J. Am. Chem. Soc.* **134** (2012) 4072–4075.
- [14] V. Maurino, C. Minero, G. Mariella, E. Pelizzetti, *Chem. Commun.* **262** (2005) 7–2629.
- [15] V. Diesen, M. Jonsson, *J. Phys. Chem. C* **118** (2014) 10083–10087.
- [16] D. Tskamoto, A. Shiro, Y. Shiraishi, Y. Sugano, S. Ichikawa, S. Tanaka, T. Hirai, *ACS Catal.* **2** (2012) 599–603.
- [17] X.J. Ye, Y.J. Cui, X.Q. Qiu, X.C. Wang, *Appl. Catal. B: Environ.* **152–153** (2014) 383–389.
- [18] D.F. Wang, T. Kako, J.H. Ye, *J. Am. Chem. Soc.* **130** (2008) 2724–2725.
- [19] X.C. Wang, K. Maeda, A. Thomas, K. Takanabe, G. Xin, J.M. Carlsson, K. Domen, M. Antonietti, *Nat. Mater.* **8** (2009) 76–80.
- [20] X.C. Wang, K. Maeda, X.F. Chen, K. Takanabe, K. Domen, Y.D. Hou, X.Z. Fu, M. Antonietti, *J. Am. Chem. Soc.* **131** (2009) 1680–1681.
- [21] F.Z. Su, S.C. Mathew, G. Lipner, X.Z. Fu, M. Antonietti, S. Blechert, X.C. Wang, *J. Am. Chem. Soc.* **132** (2010) 16299–16301.
- [22] G.H. Dong, L.Z. Zhang, *J. Phys. Chem. C* **117** (2013) 4062–4068.
- [23] G.H. Dong, Z.H. Ai, L.Z. Zhang, *Water Res.* **66** (2014) 22–30.
- [24] Y. Shiraishi, S. Kanazawa, Y. Kofuji, H. Sakamoto, S. Ichikawa, S. Tanaka, T. Hirai, *Angew. Chem. Int. Ed.* **53** (2014) 13454–13459.
- [25] S.C. Yan, Z.S. Li, Z.G. Zou, *Langmuir* **26** (2010) 3894–3910.
- [26] S.C. Yan, Z.S. Li, Z.G. Zou, *Langmuir* **25** (2009) 10397–10401.
- [27] G.H. Dong, W.K. Ho, Y.H. Li, L.Z. Zhang, *Appl. Catal. B: Environ.* **174** (2015) 477–485.
- [28] Q.J. Xiang, J.G. Yu, M. Jaroniec, *J. Phys. Chem. C* **115** (2011) 7355–7363.
- [29] J.G. Yu, K. Wang, W. Xiao, B. Cheng, *Phys. Chem. Chem. Phys.* **16** (2014) 11492–11501.
- [30] A.L. Linsebigler, G.Q. Lu, J.T. Yates, *Chem. Rev.* **95** (1995) 735–758.
- [31] Y.H. Lv, Y.F. Liu, Y.Y. Zhu, Y.F. Zhu, *J. Mater. Chem. A* **2** (2014) 1174–1182.
- [32] D.M. Chen, Z.H. Wang, T.Z. Ren, D. Hao, W.Q. Yao, R.L. Zong, Y.F. Zhu, *J. Phys. Chem. C* **118** (2014) 15300–15307.
- [33] H. Li, J. Shang, Z.H. Ai, L.Z. Zhang, *J. Am. Chem. Soc.* **137** (2015) 6393–6399.
- [34] G.H. Dong, W.K. Ho, C.Y. Wang, *J. Mater. Chem. A* **3** (2015) 23435–23441.
- [35] C.Z. Zhang, R. Hao, H.B. Liao, Y.L. Hou, *Nano Energy* **2** (2013) 88–97.
- [36] G.H. Dong, Z.H. Ai, L.Z. Zhang, *RSC Adv.* **4** (2014) 5553–5560.
- [37] L. Wang, M.H. Cao, Z.H. Ai, L.Z. Zhang, *Environ. Sci. Technol.* **48** (2014) 3354–3362.
- [38] P. Niu, L.C. Yin, Y.Q. Yang, G. Liu, H.M. Cheng, *Adv. Mater.* **26** (2014) 8046–8052.